Role of Rydberg States in the Photochemical Dynamics of Ethylene

4 AUTHORS:

Toshifumi Mori
Institute for Molecular Science
16 PUBLICATIONS **173** CITATIONS

SEE PROFILE

William James Glover
University of California, Los Angeles
21 PUBLICATIONS **404** CITATIONS

SEE PROFILE

Michael S Schuurman
National Research Council Canada
37 PUBLICATIONS **578** CITATIONS

SEE PROFILE

Todd J. Martinez
Stanford University
239 PUBLICATIONS **7,866** CITATIONS

SEE PROFILE

Role of Rydberg States in the Photochemical Dynamics of Ethylene

Toshifumi Mori,[†,‡] William J. Glover,[†,‡] Michael S. Schuurman,[§] and Todd J. Martinez[*,†,‡]

[†]PULSE Institute and Department of Chemistry, Stanford University, Stanford, California 94305, United States

[‡]SLAC National Accelerator Laboratory, 2575 Sand Hill Road, Menlo Park, California, United States

[§]Steacie Institute for Molecular Sciences, National Research Council of Canada, Ottawa, Canada

Ⓢ *Supporting Information*

ABSTRACT: We use the ab initio multiple spawning method with potential energy surfaces and nonadiabatic coupling vectors computed from multistate multireference perturbation theory (MSPT2) to follow the dynamics of ethylene after photoexcitation. We introduce an analytic formulation for the nonadiabatic coupling vector in the context of MSPT2 calculations. We explicitly include the low-lying 3s Rydberg state which has been neglected in previous ab initio molecular dynamics studies of this process. We find that although the 3s Rydberg state lies below the optically bright $\pi\pi^*$ state, little population gets trapped on this state. Instead, the 3s Rydberg state is largely a spectator in the photodynamics, with little effect on the quenching mechanism or excited state lifetime. We predict the time-resolved photoelectron spectrum for ethylene and point out the signature of Rydberg state involvement that should be easily observed.
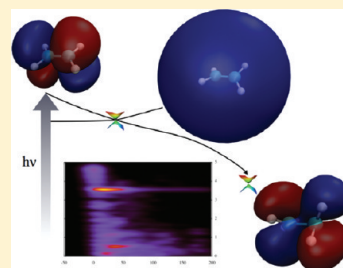
I. INTRODUCTION

Photoinduced *cis−trans* isomerization has been a central topic in the study of photochemical reactions over the past decades. For example, the photoisomerization in the retinal protonated Schiff base (RPSB) is known to be the initial step of vision,[1] and the green fluorescent protein (GFP) chromophore in solution shows a fast decay through isomerization,[2] remarkably different from its fluorescent behavior in the protein environment.[3] These ultrafast decay mechanisms are often understood in the context of conical intersections (CIs), that is, true crossings of two (or more) electronic states where nonadiabatic transitions occur efficiently.[4,5] These photoisomerization reactions can efficiently convert photon energy into mechanical motion on the molecular scale, motivating a detailed understanding of the reaction dynamics.

The ethylene molecule has been considered to be a prototype of such photoisomerization reactions. Due to its simple geometry and very short excited state lifetime following photoexcitation to the spectroscopically bright $\pi\pi^*$ state, there have been many experimental[6−12] and theoretical[4,13−19] studies of the excited state dynamics. The excited state lifetime inferred from time-resolved photoionization experiments was approximately 50 fs,[6−9] while most previous theoretical calculations estimated it to be somewhat longer, ranging from 89 to 180 fs.[13−15,19] A direct comparison of the photoion signals from experiment and simulation[16] suggested that the discrepancy between theory and experiment may be attributed to effects arising from the energy of the experimental probe pulse, pointing out the need for further careful and detailed comparisons to fully understand the dynamics. The molecular mechanism for the ground state decay process has also been discussed,[4,15,17−21] focusing mainly on two types of CIs, that is, the twisted-pyramidalized (Tw-Py) and

ethylidene-type (Et) CIs. The existence of a CI seam hypersurface connecting the two CI minima has also been pointed out,[18,20,22] but its relevance during the dynamics has not been fully elucidated.

The existence of Rydberg states that could potentially influence the dynamics has been recognized in previous theoretical studies. Spectroscopic lines due to Rydberg states are embedded in the broad $\pi\pi^*$ absorption,[23−26] but the π-3s Rydberg state is located well below the $\pi\pi^*$ absorption maximum and is separated from the other π-3p Rydberg states. Previous work has assumed that the Rydberg states are primarily spectators during the dynamics and that they may be safely ignored.[13−16] However, there is as of yet no direct dynamical study of their influence to corroborate this assumption. Thus, the relevance of the Rydberg states remains an open question, which we address here with ab initio multiple spawning (AIMS) molecular dynamics using electronic structure methods that incorporate dynamic electron correlation effects.

The difficulty of performing direct dynamics simulations including both Rydberg and valence electronic states stems from the need to maintain a balanced description of states of very different character. Diffuse basis functions are needed to describe the extended orbitals involved in the Rydberg states, but also dynamic electron correlation effects are known to be crucial,[18,20] mandating an electronic structure method beyond complete active space self-consistent-field (CASSCF) such as the multistate

second order perturbation (MSPT2) theory.[27] Although the MSPT2 method was used some time ago for minimal energy conical intersection optimization,[28] it has only recently been used in nonadiabatic dynamics simulations.[15] However, the lack of analytical nonadiabatic coupling vectors at the MSPT2 level has been an obstacle to widespread use for both intersection optimization and nonadiabatic dynamics. Here, we present formulas for analytical MSPT2 nonadiabatic couplings and discuss their implementation within the AIMS method to perform nonadiabatic dynamics at the MSPT2 level. In the present work, we focus on the interplay of the valence $\pi\pi^*$ and π-3s Rydberg states during the nonadiabatic dynamics of photoexcited ethylene. For this purpose, we introduce a basis set designed to describe the 3s diffuse orbital as well as the valence states and validate our choice of basis, active space, and MSPT2 electronic structure against higher-level multireference configuration interactions calculations. Our dynamics simulations reveal that partial population transfer from the valence to Rydberg state occurs on a rapid time scale ($\sim$10 fs); however, the Rydberg population is short-lived (<60 fs) and has only a modest influence on the predicted excited-state lifetime of ethylene (as assumed in previous work). Finally, the time-resolved photoelectron spectrum[29,30] is calculated to show how the π-3s Rydberg state might be identified in experiments designed to test the predictions we present here.

II. THEORETICAL METHODS

A. Ab Initio Multiple Spawning. Since the details of the ab initio multiple spawning (AIMS) method have been described elsewhere,[15,31] we only give a brief summary to provide the necessary background to describe our implementation of MSPT2 electronic structure within the AIMS framework.

In the AIMS method, the total wave function of a molecule at time t is given by a sum over different electronic states

$$\Psi(\mathbf{r}, \mathbf{R}, t) = \sum_I \chi_I(\mathbf{R}, t)\phi_I(\mathbf{r}; \mathbf{R}) \tag{1}$$

Here, $\mathbf{r}$ and $\mathbf{R}$ denote the electronic and nuclear coordinates, I is the electronic state index, and $\chi_I(\mathbf{R}, t)$ and $\phi_I(\mathbf{r}; \mathbf{R})$ are the nuclear and electronic wave functions, respectively. The nuclear wave function is further decomposed into a superposition of complex frozen Gaussian nuclear trajectory basis functions (TBFs)

$$\chi_I(\mathbf{R}, t) = \sum_i c_I^i(t)\chi_I^i(\mathbf{R}, \overline{\mathbf{R}}_I^i(t), \overline{\mathbf{P}}_I^i(t), \gamma_I^i(t)) \tag{2}$$

where i is the index of a TBF and $c_I^i(t)$, $\overline{\mathbf{R}}_I^i(t)$, $\overline{\mathbf{P}}_I^i(t)$, and $\gamma_I^i(t)$ denote the complex amplitude, position, momentum, and phase of the ith TBF (associated with the Ith electronic state), respectively. The width parameters of the frozen Gaussian TBFs are isotropic and depend only on the atomic mass, with specific values chosen according to previous work.[32] The phase space centers of the TBFs, $\overline{\mathbf{R}}_I^i(t)$ and $\overline{\mathbf{P}}_I^i(t)$, evolve according to classical equations of motion where the potential energy and force are calculated on the fly. The TBF phase $\gamma_I^i(t)$ is propagated semiclassically, and complex amplitudes $c_I^i(t)$ are determined by solving the time-dependent Schrödinger equation within the basis of TBFs:

$$\sum_J \sum_j \delta_{IJ} \left(\langle \chi_I^i | \chi_J^j \rangle_R \frac{\partial c_J^j}{\partial t} + c_J^j \left\langle \chi_I^i \left| \frac{\partial}{\partial t} \chi_J^j \right\rangle_R \right) = -i \sum_J \sum_j H_{IJ}^{ij} c_J^j \tag{3}$$

Here $\langle \cdots \rangle_R$ denotes the integral over nuclear coordinates and H_{IJ}^{ij} is the Hamiltonian matrix element. Because we are using adiabatic

electronic states, H_{IJ}^{ij} can be simplified to[33]

$$H_{IJ}^{ij} \simeq \left\langle \chi_I^i | \hat{T}_{nuc} | \chi_J^j \right\rangle_R \delta_{IJ} + \left\langle \chi_I^i | V_I | \chi_J^j \right\rangle_R \delta_{IJ}$$

$$+ (1 - \delta_{IJ}) \sum_A^{N_{atoms}} \frac{1}{2m_A} \sum_{\sigma = x,y,z} \mathbf{d}_{IJ,A_\sigma}^{el} \left\langle \chi_I^i \left| \frac{\partial}{\partial \mathbf{R}_{A_\sigma}} \right| \chi_J^j \right\rangle_R \tag{4}$$

where $\hat{T}_{nuc}$ is the nuclear kinetic energy operator, A is the atom index, m_A is mass of atom A, V_I is the potential energy surface for the Ith adiabatic electronic state, and $\mathbf{d}_{IJ,A}^{el}$ is the nonadiabatic coupling vector between electronic states I and J. We have neglected the higher order (second derivative) nonadiabatic coupling terms, following the usual practice. As can be seen from eqs 3 and 4, population transfer between electronic states I and J results when the nonadiabatic coupling vector $\mathbf{d}_{IJ,a}^{el}$ is large. The multidimensional integral over the nuclear wave function in eq 4 implies knowledge of V_I and $\mathbf{d}_{IJ,a}^{el}$ at all molecular configurations, but by making use of the localized nature of the TBFs, one can approximate the integral using a saddle point approximation (SPA). This gives

$$H_{IJ}^{ij} \simeq \left\langle \chi_I^i \left| \hat{T}_{nuc} \right| \chi_J^j \right\rangle_R \delta_{IJ} + \left\langle \chi_I^i \left| \chi_J^j \right\rangle_R V_I(\tilde{\mathbf{R}}) \delta_{IJ} \right.$$

$$+ (1 - \delta_{IJ}) \sum_A^{N_{atoms}} \frac{1}{2m_A} \sum_{\sigma = x,y,z} \mathbf{d}_{IJ,A_\sigma}^{el}(\tilde{\mathbf{R}}) \left\langle \chi_I^i \left| \frac{\partial}{\partial \mathbf{R}_{A_\sigma}} \right| \chi_J^j \right\rangle_R \tag{5}$$

where $\tilde{\mathbf{R}}$ is the position of the centroid of TBFs I and J.[15]

The central goal of the AIMS method is to simulate nonadiabatic events from first principles, that is, without a priori knowledge of the potential energy surfaces or their intersections. This implies that the TBF basis set expansion of the molecular wavepacket in eq 2 should be sufficiently flexible to allow population transfer between states when regions of strong coupling are visited by the wavepacket. In AIMS, this flexibility is attained by adaptively increasing the number of TBFs, in a process called spawning, when the coupling of two states rises above a predefined threshold. As discussed in detail previously,[15,31,34] the nonadiabatic coupling vectors are used in AIMS in three ways: (1) to construct the Hamiltonian matrix elements in eq 5, (2) to decide when spawning occurs, and (3) to determine the momentum of the newly created child TBF's following spawning. In the first two uses, one does not need the entire nonadiabatic coupling vector but rather only the dot product with a (complex) off-diagonal matrix element of the momentum operator. Hence, finite difference schemes can be used quite effectively, requiring only a few evaluations of the MSPT2 energy. Unfortunately, the last use of the nonadiabatic coupling vector requires knowledge of all components and, thus, finite difference evaluation would require $3N_{atoms}$ evaluations of the MSPT2 energy. This last use of the nonadiabatic coupling vector allows one to ensure that the classical energy of the child TBF matches that of its parent. Typically, this is achieved by scaling the momentum of the child TBF along the direction of the nonadiabatic coupling vector, which has been justified semiclassically.[35] However, the lack of a full nonadiabatic coupling vector at the MSPT2 level limited the previous work to instead scaling the child TBF momentum along the energy difference gradient direction.[15] In the context of surface-hopping methods, this alternate choice can sometimes have an adverse effect on the agreement of the results with quantum mechanical simulations.[36] Although one expects the

dependence to be less in the AIMS method since the TBFs have a finite position and momentum width, one would nevertheless prefer the choice that has a firm semiclassical footing. Below we provide the analytical formula for the MSPT2 nonadiabatic coupling vector implemented in this work and used for the momentum adjustment of child TBFs.

B. Analytical Nonadiabatic Coupling Vectors from MSPT2. In the MSPT2 method,[27] the energy and the wave function of an electronic state I at nuclear coordinate $\mathbf{R}$ is given by

$$E_I(\mathbf{R}) = H_{IJ}^{el}(\mathbf{R}) = \sum_{M,N} u_M^I(\mathbf{R}) H_{MN}^{eff}(\mathbf{R}) u_N^J(\mathbf{R}) \tag{6}$$

and

$$\left| \phi_I^{MSPT2}(\mathbf{R}) \right\rangle = \sum_M u_M^I(\mathbf{R}) \left\{ \left| \phi_M^{(0)}(\mathbf{R}) \right\rangle + \left| \phi_M^{(1)}(\mathbf{R}) \right\rangle \right\} \tag{7}$$

Here, the subscript M is the CASSCF state index, H_{MN}^{eff} is the CASPT2 effective Hamiltonian, u_M^I is the MSPT2 mixing coefficient obtained by diagonalizing H_{MN}^{eff}, and $\left| \phi_M^{(0)} \right\rangle$ and $\left| \phi_M^{(1)} \right\rangle$ are CASSCF and first order CASPT2 wave functions, respectively (for simplicity hereafter, we drop the nuclear coordinate label $\mathbf{R}$). Any MSPT2 property, A_{IJ}^{MSPT2}, can then be approximated from a perturbation-modified CAS reference function,[27] that is,

$$A_{IJ}^{MSPT2} \simeq \sum_{M,N} u_M^I \left\langle \phi_M^{(0)} \left| \hat{A} \right| \phi_N^{(0)} \right\rangle_r u_N^J \tag{8}$$

Thus, the nonadiabatic coupling for the MSPT2 method is given by

$$\begin{aligned}
\mathbf{d}_{IJ,a}^{el} &= \sum_M u_M^I \frac{\partial u_M^J}{\partial \mathbf{R}_a} + \sum_{M,N} u_M^I u_N^J \left\langle \phi_M^{(0)} \left| \frac{\partial}{\partial \mathbf{R}_a} \right| \phi_N^{(0)} \right\rangle_r \\
&= (E_J - E_I)^{-1} \sum_{M,N} u_M^I u_N^J \frac{\partial H_{MN}^{eff}}{\partial \mathbf{R}_a} + \sum_{M,N} u_M^I u_N^J \left\langle \phi_M^{(0)} \left| \frac{\partial}{\partial \mathbf{R}_a} \right| \phi_N^{(0)} \right\rangle_r
\end{aligned} \tag{9}$$

The first term in eq 9 is the derivative of the MSPT2 mixing coefficients, which we evaluate analytically in a similar manner as the energy gradients[37,38] by realizing that

$$\begin{aligned}
2 \sum_{M,N} u_M^I u_N^J \frac{\partial H_{MN}^{eff}}{\partial \mathbf{R}_a} &= \sum_{M,N} (u_M^I + u_M^J) \frac{\partial H_{MN}^{eff}}{\partial \mathbf{R}_a} (u_N^I + u_N^J) \\
&\quad - \sum_{M,N} u_M^I \frac{\partial H_{MN}^{eff}}{\partial \mathbf{R}_a} u_N^I - \sum_{M,N} u_M^J \frac{\partial H_{MN}^{eff}}{\partial \mathbf{R}_a} u_N^J
\end{aligned} \tag{10}$$

Here the first term refers to the energy gradient of a "mixed" state (formed by adding together the mixing coefficients of states I and J) while the second and third terms are the energy gradients of states I and J. The second term in eq 9 is included as a correction arising from nuclear derivatives of the CASSCF wave function. The first term in eq 9 is dominant for molecular configurations near conical intersections, but contributions from the second term can become comparable when the energy gap between the two states becomes large.

C. Time-Resolved Photoelectron Spectra. Our AIMS method, described above, provides a means of simulating the time evolution of the nuclear wave function for ethylene following

electronic excitation and we have shown previously how to extract a time-resolved photoelectron spectrum (TRPES) from this information.[39] Here we briefly review our approach, developed previously for CASSCF electronic wave functions,[39] and highlight the modifications we made to incorporate MSPT2 electronic structure information.

We start by considering ionization of a localized wavepacket described by a single TBF on neutral state I. From Fermi's Golden Rule, and assuming the ionization is fully vertical, the single-photon ionization probability is

$$\begin{aligned}
P_{I-\alpha\eta}(t) &\propto \omega_{probe} \left| \left\langle \phi_I \left| \vec{\varepsilon} \cdot \hat{\mu} \right| \phi_\alpha \psi_\eta \right\rangle \right|^2 \\
&\quad \times \delta \left(\hbar\omega_{probe} - IP_{I-\alpha}(\mathbf{R}(t)) - E_k(\eta) \right)
\end{aligned} \tag{11}$$

where $\left| \phi_\alpha \right\rangle$ is the electronic wave function of cation state α, ψ_η is the photoelectron orbital with combined-quantum state η (comprising wavevector k and angular momentum lm), $\hbar\omega_{probe}$ is the energy of the probe laser, $\vec{\varepsilon}$ is the laser polarization, and $\hat{\mu}$ is the molecular dipole operator. The ionization potential, $IP_{I-\alpha}(\mathbf{R})$, is given by the energy difference between cation state α and neutral state I at molecular geometry $\mathbf{R}$. Finally, E_k is the kinetic energy of the photoelectron ($E_k = k^2/2$), which is the experimental observable of interest.

According to eq 11, there are two factors that control the photoelectron intensity: (i) the resonance condition that ensures energy conservation before and after ionization and (ii) the photoelectron matrix element that determines the optical brightness of the transition. Under the assumption that the photoelectron orbital is orthogonal to the occupied neutral orbitals, the photoelectron intensity becomes

$$\begin{aligned}
P_{I-\alpha\eta}(t) &\propto \omega_{probe} \left| \left\langle \psi_{I-\alpha}^d \left| \vec{\varepsilon} \cdot \hat{\mu} \right| \psi_\eta \right\rangle \right|^2 \\
&\quad \times \delta \left(\hbar\omega_{probe} - IP_{I-\alpha}(\mathbf{R}(t)) - E_k(\eta) \right)
\end{aligned} \tag{12}$$

where $\psi_{I-\alpha}^d$ is a Dyson orbital, defined as

$$\psi_{I-\alpha}^d = \sqrt{N} \int dr_1 \cdots dr_{N-1} \phi_1^*(r_1 \cdots r_N) \phi_\alpha(r_1 \cdots r_{N-1}) \tag{13}$$

We showed previously how Dyson orbitals in eq 13 can be calculated from CASSCF wave functions by expanding both the neutral and the cation states in a common set of orbitals corresponding to the neutral molecule.[39] To extend this approach for MSPT2 wave functions, we follow eq 8 and evaluate the Dyson orbital using perturbation-modified reference wave functions, that is,

$$\psi_{I-\alpha}^d = \sqrt{N} \sum_{m,n} u_m^I u_n^\alpha \int dr_1 \cdots dr_{N-1} \phi_m^{(0)}(r_1 \cdots r_N) \phi_n^{(0)}(r_1 \cdots r_{N-1}) \tag{14}$$

where we have suppressed complex conjugation because the wave functions are real valued. To evaluate the photoelectron matrix element in eq 12, we work in the limit that the continuum electron interacts with the ionized molecule only through a point charge Coulomb potential, such that the continuum functions, ψ_η, correspond to Coulomb partial waves. The integral in eq 12 is then evaluated on a real space grid using the ezDyson code,[40−42]

2810

dx.doi.org/10.1021/jp2097185 |*J. Phys. Chem. A* 2012, 116, 2808–2818

which includes isotropic angular averaging of the photoelectron matrix element. Finally, we calculate the vertical ionization energies in eq 12 at the MSPT2 level, including a constant energetic shift to bring the electron kinetic energies at the Franck–Condon point in coincidence with experiment, as described previously.[39]

Having calculated the photoelectron signal for a single basis function, we follow a semiclassical prescription and define the total time-resolved photoelectron spectrum as an incoherent sum of the contributions from each TBF, weighted by their nuclear populations:

$$P(E_k, t) \propto \frac{\omega_{probe}}{k} \sum_{I, i, \alpha, \eta} n_i^I(t) \left| \left\langle \psi_{I-\alpha}^d | \vec{\varepsilon} \cdot \hat{\mu} | \psi_\eta \right\rangle \right|^2$$
$$\times \delta\left(\hbar\omega_{probe} - IP_{I-\alpha}(\mathbf{R}_i^I(t)) - E_k(\eta)\right) \quad (15)$$

where the $1/k$ multiplicative factor at the front of eq 15 comes from the change of variables from wavevector to energy: $dE_k = kdk$.

III. COMPUTATIONAL DETAILS

In the present study, the 6-31G* basis set used previously[15] was adopted to describe the valence states. To also describe the low-lying 3s Rydberg state, we have augmented the basis set with a single primitive s Gaussian orbital placed midway between the two carbon atoms.[27] The exponent of this orbital was set to 0.0208 (in atomic units), which was determined by fitting the energy of the π-3s Rydberg [Ryd(3s) in Mulliken notation] state at the Franck–Condon (FC) and Ryd(3s)/$\pi\pi^*$ intersection geometries to previous computational and experimental results.[18,20,24,43,44] Details of the fitting procedure are provided in Supporting Information. The CASSCF active space consisted of three orbitals (π, π^*, and 3s) with two electrons. State averaging was performed over five states (SA5-CASSCF), that is, the $(\pi)^2$, $\pi\pi^*$ and $(\pi^*)^2$ valence states as well as the π-3s and π^*-3s Rydberg states. The π^*-3s Rydberg state was included for two reasons: First, this state is required to describe the torsion around the C=C bond up to 180°, because it becomes degenerate with the Ryd(3s) (π-3s) state at a 90° twisted geometry. Second, the CASSCF energy of the π^*-3s state at the FC geometry is lower than that of the valence $(\pi^*)^2$ state, which is corrected only after dynamic electron correlation is included at the CASPT2 level.

The initial conditions (positions and momenta) for the dynamics were Monte Carlo sampled from the ground state $\nu = 0$ vibrational Wigner distribution within the harmonic approximation. All the TBFs were initially excited to the S_2 state ($\pi\pi^*$ character around FC region) and were propagated with a time step of ~0.24 fs (10 atomic time units) for up to 200 fs. Because our focus is on the excited-state dynamics, TBFs that were spawned to the ground state were not further propagated once they became uncoupled from other TBFs. For comparison, we also ran the dynamics without Rydberg states and the diffuse orbital using the same initial conditions, hereafter referred to as valence-only calculations. A total of 37 initial TBFs were prepared and run independently in each case and by the end, 801 and 114 TBFs were spawned for the Rydberg and valence-only calculations respectively.

Using the neutral wave packet dynamics obtained from the AIMS simulations, the TRPES was calculated with a probe energy of 7.0 eV and convolved in both energy and time domains with Gaussian functions having full widths at half-maxima
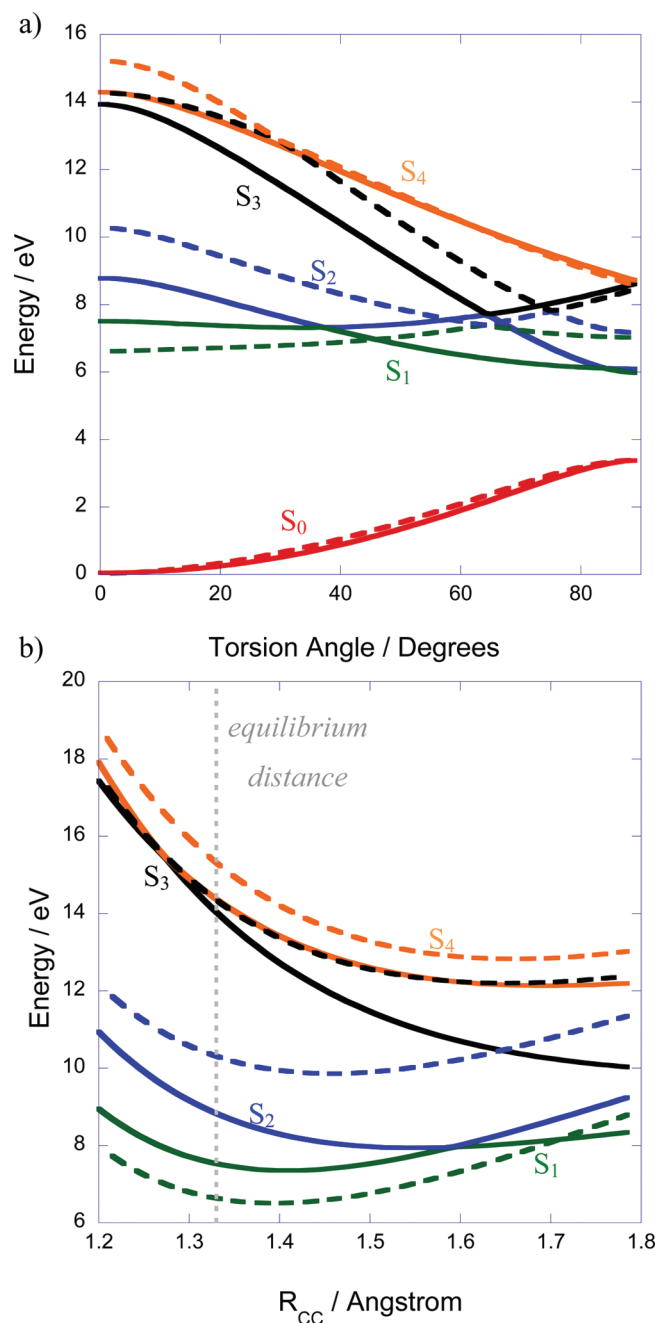

Figure 1. Potential energy curves along (a) the H–C–C–H torsion and (b) C–C stretch coordinates. Red, green, blue, black, and orange represent S_0, S_1, S_2, S_3, and S_4 adiabatic states, respectively. Other internal coordinates are fixed at the Franck–Condon (FC) geometry. Energies are measured from the S_0 state energy at the FC point. Solid and dotted lines are MSPT2 and CASSCF energies, respectively. The C=C bond length in the S_0 equilibrium geometry is indicated with a vertical dotted gray line in (b).

of 0.14 eV and 25 fs respectively, corresponding to typical experimental resolutions. The energy and wave function of the cation ground state were calculated with the MSPT2 method using unrelaxed orbitals from the neutral calculation. As described previously,[39,45] to ensure the calculated electron kinetic energy (difference between the probe energy and ionization potential) is in agreement with experiment for overlapping pump

and probe pulses (i.e., zero time delay), the vertical ionization energies were shifted by a constant amount. Shifts of +0.88 eV and +1.01 eV were used for the Rydberg and Valence-only calculations, respectively, which were determined by matching the neutral $\pi\pi^*$ vertical ionization energy, calculated at the ground state geometry, to experiment.[16]

Electronic structure calculations were performed using the Molpro 2006 quantum chemistry package,[46] where we implemented our AIMS and MSPT2 nonadiabatic coupling codes. The ezDyson code was used in the calculation of photoionization cross sections as described above.[40]

IV. RESULTS AND DISCUSSION

A. Potential Energy Surfaces. Before discussing the excited-state dynamics of ethylene, we first examine the character of the potential energy surfaces (PESs). The PESs along C=C torsion and C=C stretch coordinates are shown in Figure 1a and b, respectively. The vertical excitation energies to $\pi\pi^*$ and Ryd(3s) states calculated with MSPT2 are 8.73 and 7.46 eV, which are somewhat larger than the experimentally determined values or previous MRCI results obtained using larger basis sets.[18,43] Nevertheless, the shapes of the potential energy curves along the torsion coordinate in Figure 1a are in good agreement with MRCI results;[18] in particular, the crossing of the $\pi\pi^*$ and Ryd(3s) states occurs at around 35°. On the other hand, CASSCF overestimates the energy of the $\pi\pi^*$ state by about 1.5 eV, while it underestimates the Ryd(3s) state energy by about 0.8 eV. This puts the $\pi\pi^*$/Ryd(3s) intersection at around 65° twist, which is significantly more twisted (and further along the reaction coordinate) than the MSPT2 and MRCI results. Thus, the effects of dynamic electron correlation are crucial to describe both the $\pi\pi^*$ and Ryd(3s) states simultaneously.

Along the C=C stretch coordinate in Figure 1b, we see a crossing between $\pi\pi^*$ and Ryd(3s) PESs at around 1.6 Å at the MSPT2 level. This is in contrast to MR-CISD findings[18] that the $\pi\pi^*$ state is above the Ryd(3s) state along this coordinate. To confirm this, we calculated MR-CISD PESs using our current basis set and a SA5-CASSCF reference (see Figure S4 in Supporting Information), where we indeed find that the $\pi\pi^*$ state is higher than that of the Ryd(3s) state, even at 1.8 Å. However, by including quadruple-excitation corrections to the MR-CISD energy using the Davidson correction, we found that the $\pi\pi^*$ PES becomes rather flat, which is similar to the MSPT2 curve, and a crossing between $\pi\pi^*$ and Ryd(3s) states is seen at around 1.75 Å, again consistent with MSPT2. Although the PES along this stretching coordinate seems to be sensitive to the effects of dynamic electron correlation, this should be a minor issue because the PES along the torsion is much steeper compared to that of the stretch. We also note that, in the valence-only case, the potential energy curves of the ground, $\pi\pi^*$, and $(\pi^*)^2$ states match those in Figure 1, implying that the diffuse molecule-centered Gaussian orbital added to the Rydberg calculations only plays a role in describing the Rydberg state.

To further understand the reaction in terms of other coordinates, we optimized the geometries of characteristic points, that is, the S_0 and S_1(Ryd(3s)) state minima in addition to S_2/S_1 and S_1/S_0 minimum energy conical intersections (MECIs). The results are summarized in Figure 2. Here we can see that the S_1 energies at the S_1 minimum and the S_2/S_1 MECI are very similar. Indeed, the Ryd(3s) PES is very flat in the region of the S_1 minimum, and only a slight twist around the C=C bond from the
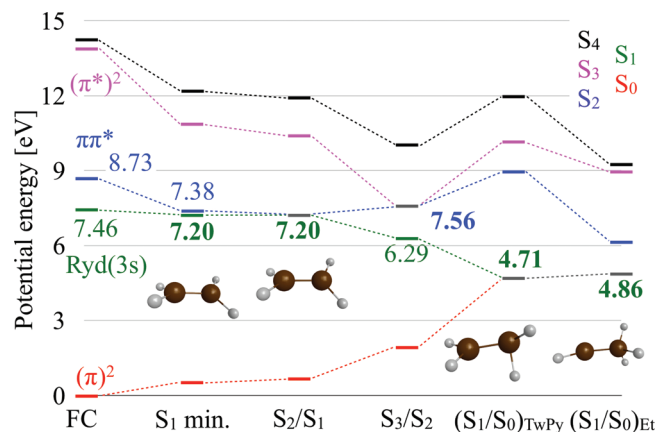

Figure 2. Energy diagram of important points during the photodynamics of ethylene. FC, S_1 min are Franck–Condon point and S_1 (Ryd(3s)) state minima, respectively, and S_2/S_1, S_3/S_2, $(S_1/S_0)_{TwPy}$, and $(S_1/S_0)_{Et}$ are minimum energy conical intersections (MECIs) connecting the indicated adiabatic states. TwPy and Et denote the twisted-pyramidalized and ethylidene-type MECIs, respectively. Optimized geometries for S_1 min, S_2/S_1, $(S_1/S_0)_{TwPy}$, and $(S_1/S_0)_{Et}$ are also shown in the figure. Adiabatic states are colored as defined in the legend, and the diabatic character of the states at the FC point is also labeled.

Ryd(3s) minimum brings the $\pi\pi^*$ state below the Ryd(3s) state. Figure 2 also shows that the twisted-pyramidalized (Tw-Py) MECI is (slightly) lower in energy than the ethylidene (Et) MECI. Barbatti et al.[18] obtained the reverse energetic ordering using MRCI-SD. However, they found this energetic ordering to switch when adding the quadruple excitation correction (MRCI-SD+Q). This again implies that MRCI-SD may be inadequate at describing dynamic electron correlation effects in ethylene for the parts of the potential energy surfaces that are relevant to the dynamics after $\pi\pi^*$ excitation (at least with the present basis set and active space). Finally, we point out that since ethylene is initially excited to the $\pi\pi^*$ state, which has an energy much higher than the MECIs, quenching pathways involving both the Tw-Py and Et intersections are energetically accessible and their relative importance can be understood only through consideration of the dynamics.

B. Dynamics. We begin our analysis of the excited-state dynamics by plotting the time evolution of the populations on each adiabatic state in Figure 3. As seen in the figure, roughly 70% of the population is transferred to the S_1 state within the first 10 fs, and further decays to the S_0 state starting around 20 fs. The excited-state lifetime (i.e., the time taken to relax to the electronic ground state) was estimated to be 90 fs by fitting the sum of the excited-state populations to a single exponential. The valence-only dynamics yielded a shorter lifetime of 60 fs, thus, the presence of the π-3s Rydberg state appears to slightly increase the excited-state lifetime. The previous valence-only AIMS-MSPT2 dynamics (with coupling vectors computed by finite difference) gave a slightly longer lifetime of 89 fs.[15] Note that this difference is partly due to the use of a different momentum adjustment method following spawning. Indeed, under the same initial conditions as the current study, using our present analytical coupling code but with momentum adjustment along the energy difference gradient (as done in the previous study) the excited-state lifetime was increased by about 10%. This is expected since the spawned basis functions will tend to have lower (in magnitude) Hamiltonian matrix elements with the parent TBF for momentum
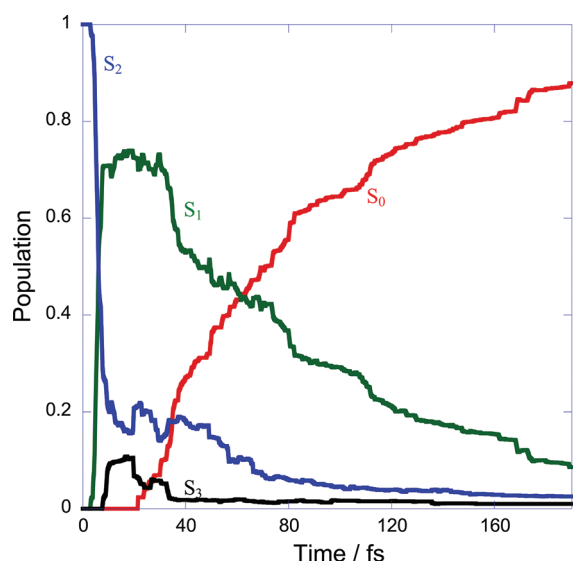
Figure 3. Time evolution of the population on the four adiabatic states, S_0 (red), S_1 (green), S_2 (blue), and S_3 (black). No population was transferred to the S_4 state.

Figure 4. Time evolution of the norm of quadrupole moments (in a.u.).

Figure 5. Time evolution of the population on valence (green) and Rydberg (blue) states averaged over initial conditions. The population of the ground state is also shown in red.

adjustments that are not along the nonadiabatic coupling vector[34] (this is the essence of the semiclassical argument[35] for using the nonadiabatic coupling vector as the momentum adjustment direction in surface hopping).

To further characterize the populations in terms of valence and Rydberg states, we calculated the isotropic second moment (Q) of the electronic wave function at each time step. Since Rydberg states are significantly more diffuse than valence states, their larger Q values distinguish them from valence states.[27] The time evolution of the distribution of Q (plotted with histogram bin widths of 0.25 fs and 1.0 atomic units) during the dynamics is shown in Figure 4. From this figure, we can see a clear distinction between the two regions centered around $Q = 31$ and $Q = 66$ atomic units, which correspond to the valence and Rydberg states respectively. Furthermore, the transitions between these two regions are found to be very rapid. Thus, we use an intermediate value of $Q = 45$ to separate the excited state populations into valence ($Q \leq 45$) and Rydberg ($Q > 45$) states. Note that because the transition is rapid, the choice of the dividing line separating valence and Rydberg states has no significant effect on the results. The time evolution of the valence and Rydberg state populations are shown in Figure 5. Now we can see that the Rydberg state is generated mostly in the first 10 fs, and about 30% of the total population transfers to the Rydberg state within this short time period. Then the population of the Rydberg state decays quickly, and within 60 fs the majority of the Rydberg state population returns to the valence state. One might ask whether the Rydberg population returns exclusively to the valence excited state or whether it can also decay directly to the ground state. As shown in Figure S6 of the Supporting Information, practically all of the population that quenches to the ground electronic state originates from excited state TBFs with valence character, that is, there is little or no decay from the Rydberg state directly to the ground electronic state.

Next, the time evolution of the geometries in the excited states is examined. We focus on the three coordinates which are expected to characterize the geometrical changes that govern population transfer:[15,18,21,31] twisting about the C=C bond
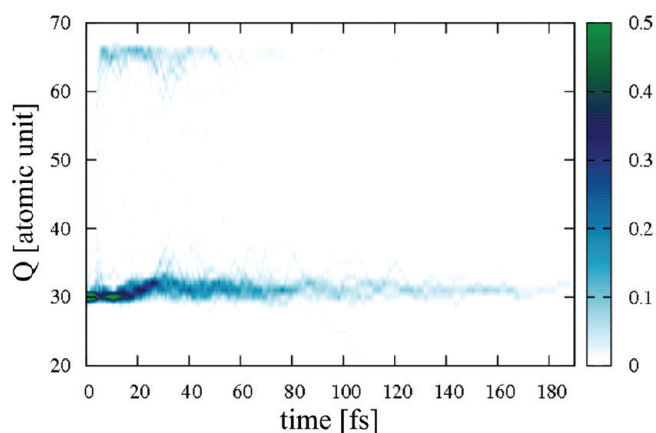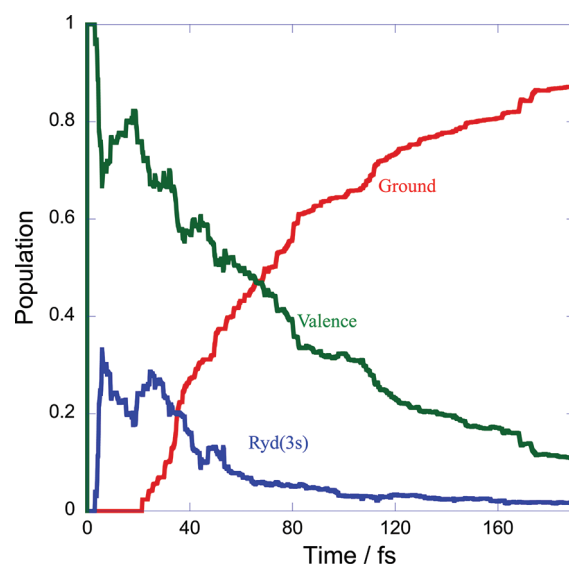
(Tw), pyramidalization of a CH_2 plane (Py), and hydrogen migration (H-mig). The time evolution of the wave packet densities projected in these three reduced coordinates was calculated using a Monte Carlo procedure,[47] and the results are shown in Figures 6–8 (the definition of each coordinate is also presented in the inset). Figure 6 shows that twisting about the C=C bond starts immediately after photoexcitation. While the majority of the TBFs on the valence states twist nearly 180° within the first 20 fs, Rydberg state TBFs are reflected at around 80°, consistent with the increasing potential with twist angle for the Rydberg state (see Figure 1a). In the valence-only dynamics, the twisting motion is more coherent since the TBFs do not spawn back and forth from the Rydberg state, but the character of the valence state dynamics remains largely the same. In Figure 7, we see that pyramidalization in the valence state TBFs also starts soon after excitation, while Rydberg state TBFs pyramidalize only to a small degree. In the valence-only dynamics, all TBFs start pyramidalizing almost immediately. Finally, Figure 8 shows that, although at least one hydrogen atom oscillates between the two carbon atoms, hydrogen transfer rarely occurs in either
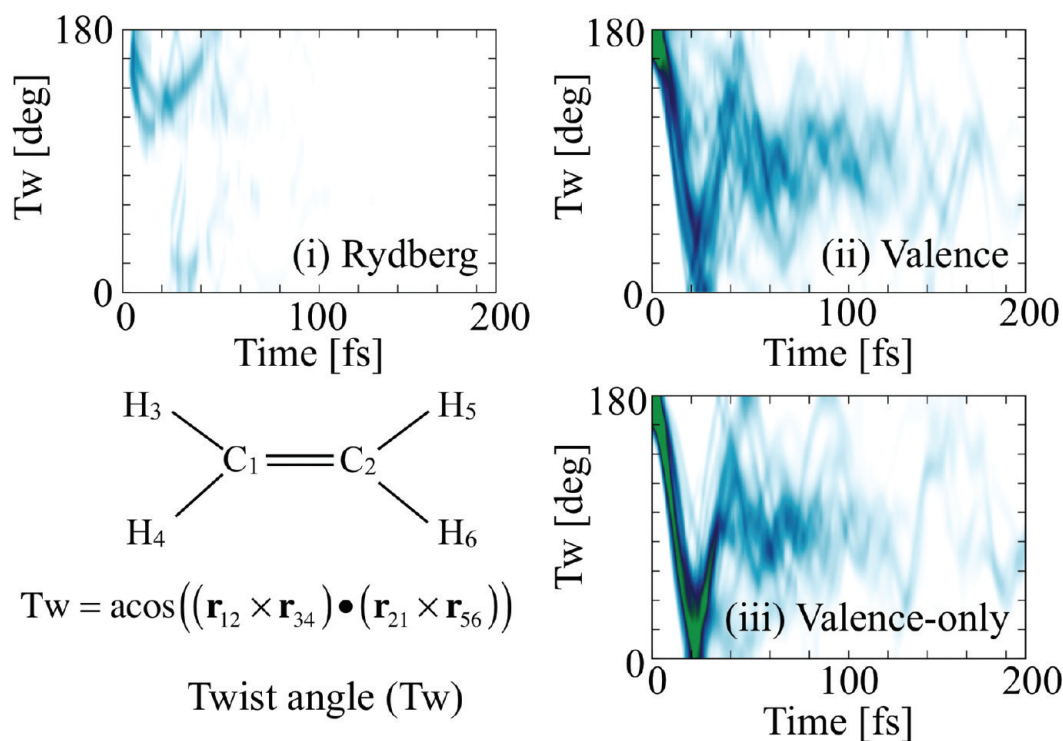
Figure 6. Time evolution of the nuclear wave packet density along the twist (Tw) coordinate. Population on Rydberg and valence states are shown in (i) and (ii), respectively. The valence state population obtained from the valence-only dynamics is also shown in (iii).
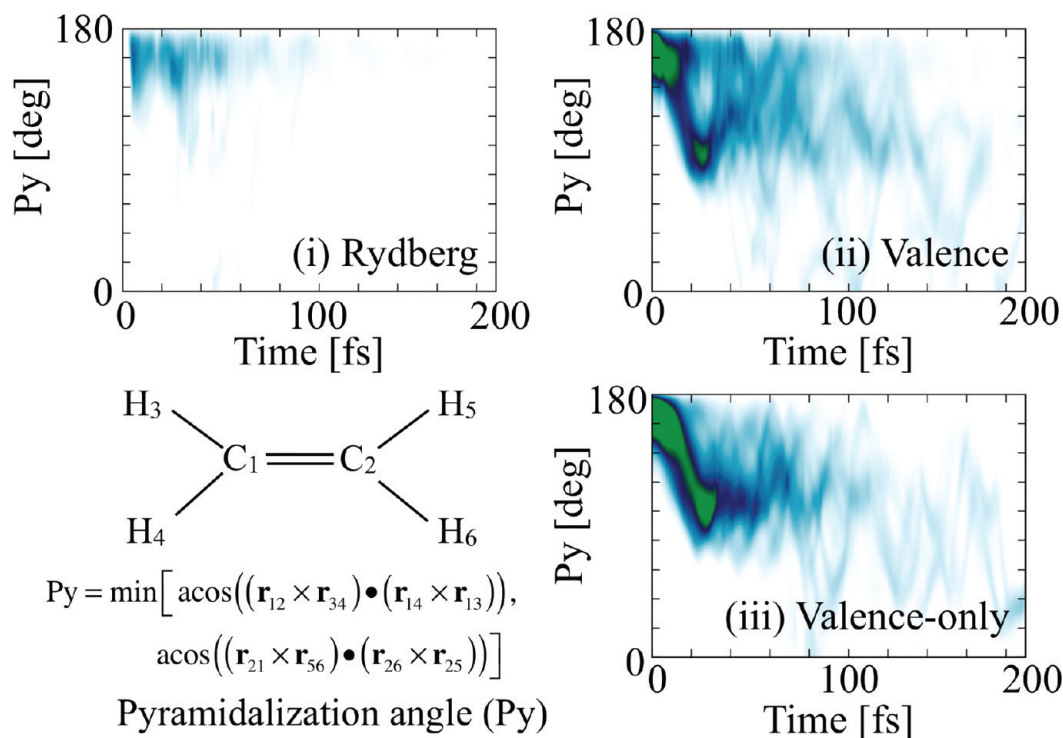

Figure 7. Same as in Figure 6, but for the pyramidalization (Py) coordinate.

the valence or Rydberg states. Hydrogen atom dissociation or exchange is not clearly revealed with this coordinate, but detailed analysis of all the excited state TBFs shows these to be very rare events and they can be safely neglected for our present purposes. Therefore, we consider that this H-mig coordinate is sufficient to describe the hydrogen migration process.
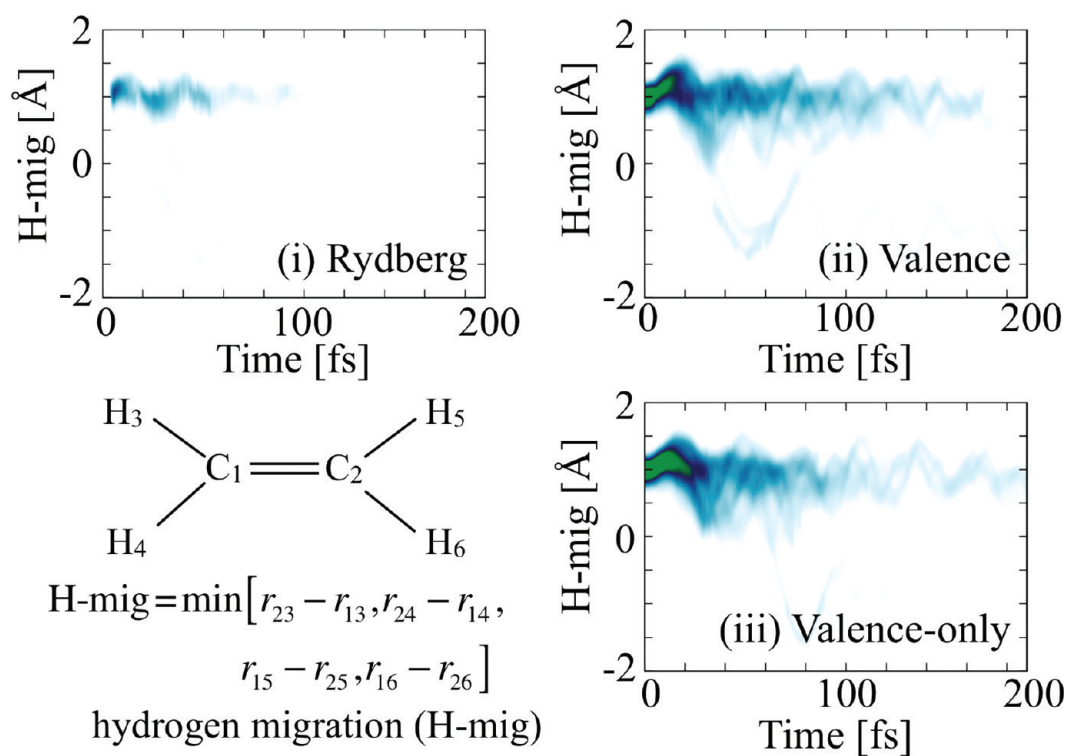
Figure 8. Same as in Figure 6, but for the hydrogen migration (H-mig) coordinate.
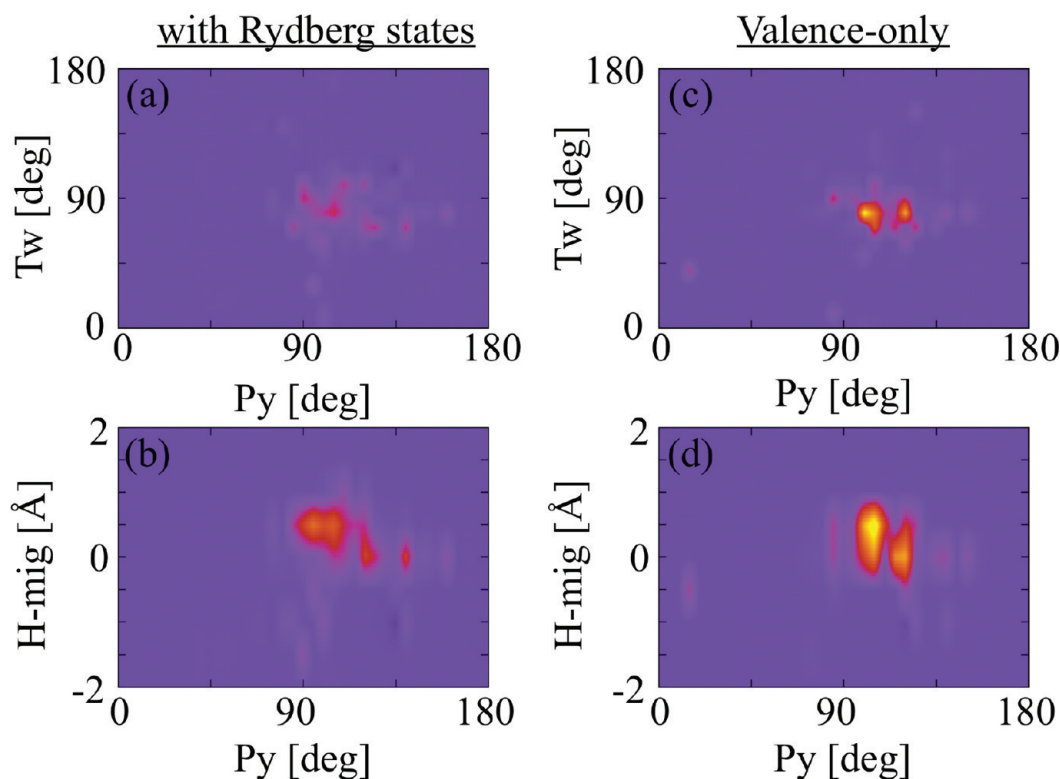

Figure 9. Distribution map of the population decay to the ground state in the reduced coordinate space. (a) and (c) are plotted against pyramidalization (Py) and twist (Tw) coordinates, while (b) and (d) are against Py and hydrogen migration (H-mig) coordinates, respectively. Left and right columns are the results with and without Rydberg states included. The geometry of each sample is taken from the center of the trajectory Gaussian basis function of the child trajectory.
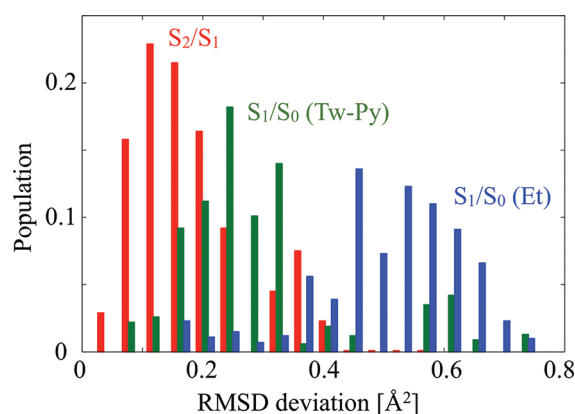
2815

dx.doi.org/10.1021/jp2097185 |*J. Phys. Chem. A* 2012, 116, 2808–2818

Figure 10. Population transfer rate as a function of the root-mean-square deviation (RMSD) from minimum energy conical intersections. The RMSD of S_2 to S_1 transition geometries from the $Ryd(3s)/\pi\pi^*$ MECI is shown in red, and the RMSD of S_1 to S_0 transition geometries from the Tw-Py MECI and Et MECI are shown in green and blue, respectively. The RMSD is measured from each trajectory Gaussian basis function of the child trajectory. Each geometry is aligned with the MECIs by taking account of permutational symmetry to minimize the RMSD value. Note that the second shoulder around 0.37 Å^2 in the S_2/S_1 plot represents the transition between $\pi\pi^*$ and $(\pi^*)^2$ states occurring at around 90° twisted geometry (see also Figure 1a).

To further elucidate the mechanism by which excited-state population returns to the ground state, we analyzed the amount of population being transferred from S_1 to S_0, $\Delta P_{S_1 \to S_0}$, as a function of the coordinates discussed above:

$$\Delta P_{S_1 \to S_0}(q_1, q_2) \equiv \int \frac{\partial P_{S_0}(\mathbf{R}; t)}{\partial t} \delta(\mathbf{R} - q_1)\delta(\mathbf{R} - q_2) \mathrm{d}t\mathrm{d}\mathbf{R}$$

(16)

Here q_1 and q_2 are the coordinates of interest, and P_{S_0} was evaluated as the change of the population on the TBF on S_0 state with its nuclear coordinates represented by the center of the Gaussian. The result is plotted in Figure 9. Here we can see that most population transfer occurs around 80−100° twisted and 80−120° pyramidalized geometries. Hydrogen migration is also seen, and moreover, roughly 40% of the population transfer occurs where the H-mig coordinate is close to zero, that is, where a hydrogen atom is equidistant from the two carbon atoms. On the other hand, only a small amount of population transfer occurs when H-mig is negative, indicating that the ethylidene-type geometry[18] is rarely involved in quenching to the ground state. To clarify this, in Figure 10 we plot the amount of population transferred as a function of the RMSD from the MECIs measured from each trajectory Gaussian center. This figure shows that population transfer occurs near molecular geometries that are closer to the Tw-Py MECI than the Et-MECI. This figure also shows that $S_1 \to S_0$ population transfer occurs in a broader range compared to $S_2 \to S_1$ population transfer, as S_1 to S_0 decay can easily occur even when the energy gap between the two states is larger than 0.50 eV.[15] From Figures 6−9, we can see that the $S_1 \to S_0$ decay in the valence-only dynamics proceeds in a very similar manner to the dynamics, including the 3s Rydberg state. These results indicate that, although the Ryd(3s) state plays a role in the initial stage of the dynamics, the mechanism for quenching to the ground state is only slightly affected. Finally we point out that the three coordinates are not orthogonal, for
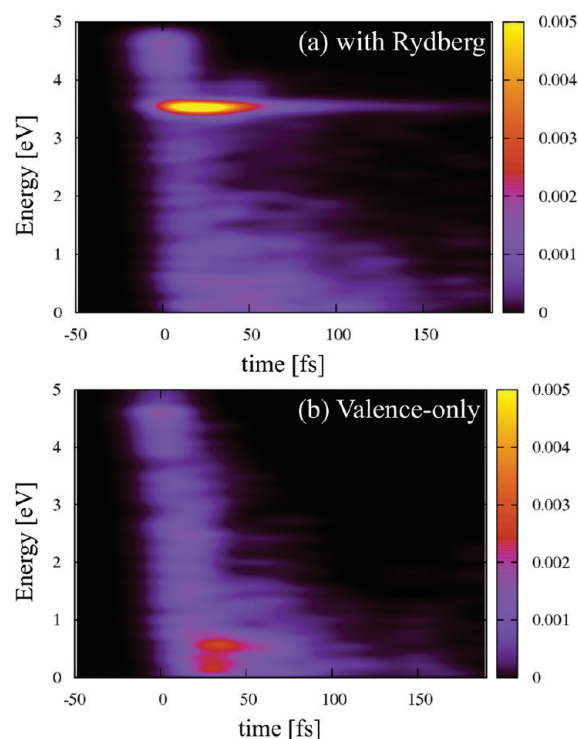

Figure 11. Time-resolved photoelectron spectra (TRPES) for the photoionization to the cation ground state calculated from (a) dynamics including Rydberg states and (b) valence-only dynamics.

example, pyramidalization motion introduces some hydrogen migration. Nevertheless, these results show that each of the three coordinates give valuable information about the dynamics and are necessary to understand the photodynamics of ethylene.

C. Time-Resolved Photoelectron Spectroscopy. Having seen that the Rydberg state is populated during the early time dynamics of photoexcited ethylene, we now consider whether there are spectroscopic signatures of the Rydberg state that might be detected in a time-resolved photoelectron spectroscopy experiment. Using the formalism described in section IIC and the AIMS dynamics results described above, we calculated the TRPES signal for excited ethylene, shown in Figure 11. Note that we only consider ionization to the cation's ground state, as the cation excited state D_1 is beyond the reach of the probe energy used here (the D_1 state at FC geometry was estimated to be 7.07 eV above D_0 with a two-state averaged MSPT2 calculation using the current basis set and active space). From Figure 11a, we see a sharp and bright peak appearing at around 3.5 eV, which decays within about 50 fs accompanied by a longer tail that lasts more than 200 fs. This sharp and bright feature corresponds to ionization from the Ryd(3s) state. Indeed, in the absence of the Rydberg state (see Figure 11b), no peak is seen in this energy region. The location of the peak from the Ryd(3s) ionization remains roughly constant in time because the Ryd(3s) PES closely parallels the D_0 state (see Figure S5 in Supporting Information), which also explains the sharpness of this peak. We can also see that after 100 fs, the spectrum above 2.0 eV disappears (except for the contribution from the Ryd(3s) state), which may imply that twisting has completed and all of the population is near the 90° twisted geometry (see the energy gap of S_1 and D_0 states in Figure S5 of Supporting Information). We also calculated the total ion yield signals from the TRPES signal
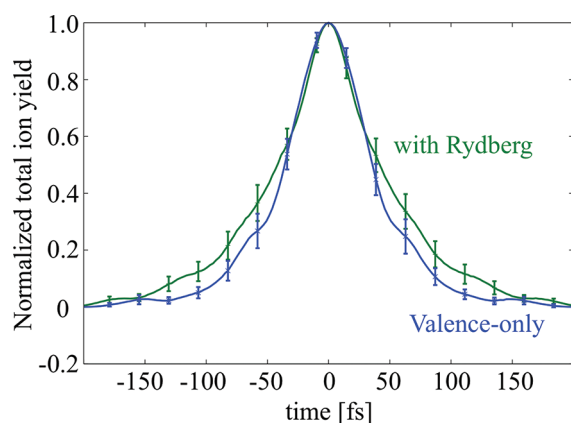
Figure 12. Normalized total ion yield signal calculated by integrating the TRPES spectra (in Figure 11) over electron kinetic energies. The full (including the Rydberg 3s state) and valence-only dynamics results are shown in green and blue, respectively, with 1σ error bars. Because the pump pulse always precedes the probe pulse in the simulation, the signal was symmetrized by adding its mirror image to represent the signal from negative time delays.

in Figure 11a,b by integrating the spectra over the plotted energy range. The results are shown in Figure 12 and demonstrate that taking account of the Rydberg states broadens the ion yield signal only slightly. Furthermore, the slight deviation is largely within the error bars ($\pm 1\sigma$, as determined by bootstrap sampling[32,48]). Thus, inclusion of the Rydberg states does not spoil the agreement with experiment reported previously.[16] This is because the population on the Rydberg state is quite low (see Figure 5), in spite of the brightness of the TRPES signal. This finding implies that it is important for pump-photoionization probe experiments to measure the ejected electron kinetic energy (i.e., the full TRPES spectrum) and not just the ion yield to fully characterize the photodynamics.

V. SUMMARY

In this paper, we studied the role of the π-3s Rydberg state (Ryd(3s)) in the photodynamics of ethylene. To describe both valence and Rydberg states simultaneously the effects of dynamic electron correlation must be included in the electronic structure method, which has been a challenge for excited-state nonadiabatic dynamics calculations that require energy gradients and nonadiabatic couplings at the same level of theory. To this end, we presented the analytic nonadiabatic couplings at the multistate CASPT2 (MSPT2) level and implemented it within the ab initio multiple spawning method. This allowed us to run nonadiabatic dynamics directly at the MSPT2 level, without resorting to postdynamics corrections, such as the common CASPT2// CASSCF approach.[49−51] Our simulations showed that wave packets initially excited to the $\pi\pi^*$ state of ethylene partially transfer to the Ryd(3s) state within the first 10 fs, but then return to the valence excited state within 60 fs. The wave packets then decay to the ground state, and the excited state lifetime was estimated to be 90 fs, which is only slightly longer than that found for simulations that do not include the Rydberg state.

By following the time evolution of the three reduced coordinates, that is, twisting about the C=C bond (Tw), pyramidalization of the CH_2 plane (Py), and hydrogen migration (H-mig), we found that Tw and Py motions start immediately after

the photoexcitation. H-mig was also observed to some extent, but a complete hydrogen transfer resulting in an ethylidene geometry while the molecule was electronically excited was rarely seen (formation of ethylidene on the ground electronic state after quenching is possible and even likely). Population transfer events were also analyzed as functions of these coordinates, and from this analysis it was found that roughly 40% of the $S_1 \rightarrow S_0$ population transfer occurs with a zero H-mig coordinate, that is, with a hydrogen atom bridging between the two carbon atoms. The results also showed that both Tw and Py motions are also important for the S_1 to S_0 decay to occur.

To make connections to experimental observables, the TRPES signal was calculated from the wave packets, where it was seen that the Rydberg state is manifested as a sharp peak, distinct from contributions from the valence states. This gives a way to directly compare the dynamics result with experiments, and we hope this work will stimulate full TRPES experiments of ethylene photodynamics.

■ ASSOCIATED CONTENT

S **Supporting Information.** Details of orbital exponent optimization for the 3s Rydberg orbital, comparison of potential energy curves obtained with MSPT2 and MRSDCI, characterization of electronic character for TBFs quenching to the ground state. This material is available free of charge via the Internet at http://pubs.acs.org.

■ ACKNOWLEDGMENT

■ REFERENCES

(1) Schoenlein, R. W.; Peteanu, L. A.; Mathies, R. A.; Shank, C. V. *Science* **1991**, *254*, 412.
(2) Usman, A.; Mohammed, O. F.; Nibbering, E. T. J.; Dong, J.; Solntsev, K. M.; Tolbert, L. M. *J. Am. Chem. Soc.* **2005**, *127*, 11214.
(3) Tsien, R. Y. *Annu. Rev. Biochem.* **1998**, *67*, 509.
(4) Levine, B. G.; Martínez, T. J. *Annu. Rev. Phys. Chem.* **2007**, *58*, 613.
(5) Yarkony, D. R. *Rev. Mod. Phys.* **1996**, *68*, 985.
(6) Farmanara, P.; Stert, V.; Radloff, S. *Chem. Phys. Lett.* **1998**, *288*, 518.
(7) Stert, V.; Lippert, H.; Ritze, H.; Radloff, W. *Chem. Phys. Lett.* **2004**, *388*, 144.
(8) Mestdagh, J.-M.; Visticot, J.-P.; Elhanine, M.; Soep, B. *J. Chem. Phys.* **2000**, *113*, 237.
(9) Kosma, K.; Trushin, S.; Fuss, W.; Schmid, W. *J. Phys. Chem. A* **2008**, *112*, 7514.
(10) Cromwell, E. F.; Stolow, A.; Vrakking, M. J. J.; Lee, Y. T. *J. Chem. Phys.* **1992**, *97*, 4029.
(11) Lin, J. J.; Wang, C. C.; Lee, Y. T.; Yang, X. *J. Chem. Phys.* **2000**, *113*, 9668.
(12) Lee, S.-H.; Lee, Y. T.; Yang, X. *J. Chem. Phys.* **2004**, *120*, 10983.
(13) Ben-Nun, M.; Martínez, T. *Chem. Phys. Lett.* **1998**, *298*, 57.
(14) Viel, A.; Krawczyk, R. P.; Manthe, U.; Domcke, W. *J. Chem. Phys.* **2004**, *120*, 11000.

2817

dx.doi.org/10.1021/jp2097185 |*J. Phys. Chem. A* 2012, 116, 2808–2818

(15) Tao, H.; Levine, B.; Martínez, T. *J. Phys. Chem. A* **2009**, *113*, 13656.

(16) Tao, H.; Allison, T. K.; Wright, T. W.; Stooke, A. M.; Khurmi, C.; van Tilborg, J.; Liu, Y.; Falcone, R. W.; Belkacem, A.; Martínez, T. J. *J. Chem. Phys.* **2011**, *134*, 244306.

(17) Ohmine, I. *J. Chem. Phys.* **1985**, *83*, 2348.

(18) Barbatti, M.; Paier, J.; Lischka, H. *J. Chem. Phys.* **2004**, *121*, 11614.

(19) Quenneville, J.; Ben-Nun, M.; Martinez, T. J. *J. Photochem. Photobiol., A* **2001**, *144*, 229.

(20) Ben-Nun, M.; Martínez, T. *Chem. Phys.* **2000**, *259*, 237.

(21) Quenneville, J.; Martinez, T. J. *J. Phys. Chem. A* **2003**, *107*, 829.

(22) Laino, T.; Passerone, D. *Chem. Phys. Lett.* **2004**, *389*, 1.

(23) Williams, B. A.; Cool, T. A. *J. Chem. Phys.* **1991**, *94*, 6358.

(24) Sension, R.; Hudson, B. *J. Chem. Phys.* **1989**, *90*, 1377.

(25) Snyder, P. A.; Atanasova, S.; Hansen, R. W. C. *J. Phys. Chem. A* **2004**, *108*, 4194.

(26) Alnama, K.; Boyé-Péronne, S.; Roche, A.; Gauyacq, D. *Mol. Phys.* **2007**, *105*, 1743.

(27) Finley, J.; Malmqvist, P.; Roos, B.; Serrano-Andrés, L. *Chem. Phys. Lett.* **1998**, *288*, 299.

(28) Levine, B. G.; Coe, J. D.; Martinez, T. J. *J. Phys. Chem. B* **2008**, *112*, 405.

(29) Stolow, A. *Adv. Chem. Phys.* **2008**, *139*, 497.

(30) Stolow, A. *Annu. Rev. Phys. Chem.* **2003**, *54*, 89.

(31) Levine, B.; Coe, J.; Virshup, A.; Martínez, T. *Chem. Phys.* **2008**, *347*, 3.

(32) Thompson, A. L.; Punwong, C.; Martinez, T. J. *Chem. Phys.* **2010**, *370*, 70.

(33) Martínez, T.; Ben-Nun, M.; Levine, R. *J. Phys. Chem. A* **1997**, *101*, 6389.

(34) Yang, S.; Coe, J. D.; Kaduk, B.; Martinez, T. J. *J. Chem. Phys.* **2009**, *130*, 134113.

(35) Herman, M. *J. Chem. Phys.* **1984**, *81*, 754.

(36) Hack, M. D.; Jasper, A. W.; Volobuev, Y. L.; Schwenke, D. W.; Truhlar, D. G. *J. Phys. Chem. A* **1999**, *103*, 6309.

(37) Mori, T.; Kato, S. *Chem. Phys. Lett.* **2009**, *476*, 97.

(38) Celani, P.; Werner, H. *J. Chem. Phys.* **2003**, *119*, 5044.

(39) Hudock, H. R.; Levine, B. G.; Thompson, A. L.; Satzger, H.; Townsend, D.; Gador, N.; Ullrich, S.; Stolow, A.; Martinez, T. J. *J. Phys. Chem. A* **2007**, *111*, 8500.

(40) ezDyson, http://iopenshell.usc.edu/downloads (accessed September 2011).

(41) Oana, C. M.; Krylov, A. I. *J. Chem. Phys.* **2007**, *127*, 234106.

(42) Oana, C. M.; Krylov, A. I. *J. Chem. Phys.* **2009**, *131*, 124114.

(43) Muller, T.; Dallos, M.; Lischka, H. *J. Chem. Phys.* **1999**, *110*, 7176.

(44) Foo, P. D.; Innes, K. K. *J. Chem. Phys.* **1974**, *60*, 4582.

(45) Hudock, H. R.; Martinez, T. J. *ChemPhysChem* **2008**, *9*, 2486.

(46) Werner, H.; Knowles, P.; Lindh, R.; Manby, F.; Schütz, M. *MOLPRO*, version 2006.1.

(47) Coe, J.; Levine, B.; Martínez, T. *J. Phys. Chem. A* **2007**, *111*, 11302.

(48) Efron, B.; Tibshirani, R. *Stat. Sci.* **1986**, *1*, 54.

(49) Celani, P.; Bernardi, F.; Robb, M.; Olivucci, M. *J. Phys. Chem.* **1996**, *100*, 19364.

(50) Sinicropi, A.; Basosi, R. *J. Phys.: Conf. Ser.* **2008**, *101*, 1.

(51) Martin, M. E.; Negri, F.; Olivucci, M. *J. Am. Chem. Soc.* **2004**, *126*, 5452.